Chiral Electrokinetic Phenomena in Single Nanopores

Kristen Alanis,[a#] *Savannah A. Silva,*[b#] *Siddharth Singh,*[c#] *Kabin Lin,*[d] *Tilman E. Schäffer,*[e] *Ovuokenye Omadoko,*[c] *John T. Fourkas,*[c,f*] *Lane. A. Baker,*[a*] *Zuzanna S. Siwy*[b*]

[a] Department of Chemistry, Texas A&M University, College Station, Texas, 77843, USA
[b] Department of Physics and Astronomy, University of California, Irvine, California, 92697, USA
[c] Department of Chemistry and Biochemistry, University of Maryland, College Park, Maryland, USA
[d] State Key Laboratory of Electromechanical Integrated Manufacturing of High-Performance Electronic Equipments, School of Mechano-Electronic Engineering, Xidian University, Xi'an 710071, People's Republic of China
[e] Institute of Applied Physics, University of Tübingen, Germany
[f] Institute for Physical Science and Technology, University of Maryland, College Park, Maryland, USA

* e-mail: fourkas@umd.edu, lane.baker@tamu.edu, and zsiwy@uci.edu
# These Authors contributed equally

Received: ((will be filled in by the editorial staff))
Accepted: ((will be filled in by the editorial staff))

Abstract
The arrangement of solvent molecules and ions at solid–liquid interfaces determines electrochemical properties that are important in separations platforms, sensing technologies, and energy-storage systems. Here we show that single glass and polymer pores in contact with propylene carbonate (PC) solutions of $LiClO_4$ exhibit an effective surface potential that is modulated by the enantiomeric excess of the solvent. In particular, electrochemical and electrokinetic measurements of ionic transport through glass pipettes and polymer pores reveal that the effective surface potential is significantly lower in solutions prepared using enantiomerically pure PC than in solutions prepared using racemic PC. Both pore systems became positively charged in all racemic solutions examined in the range of $LiClO_4$ concentrations between 1 mM and 100 mM, whereas solutions in (*R*)-(+)-PC induced a positive surface potential only at concentrations above ~5 mM. The effective surface potential is quantified through asymmetry in current–voltage curves and zeta-potential measurements. Vibrational sum-frequency-generation experiments on $LiClO_4$ solutions in racemic and enantiomerically pure PC indicate that the surface lipid-bilayer-like region in the former is more strongly organized than in the latter, dictating the favorable positions for lithium and perchlorate ions in each case. The more ordered molecular packing in the racemic liquid leads to accumulation of lithium ions on the outside of the bilayer, creating a higher effective positive charge. Our results highlight the extreme sensitivity of the interfacial potential on molecular organization of the solvent, and the relatively unexplored role that chirality can play in electrokinetic phenomena.

Keywords: ion transport, double layer, zeta potential, electrokinetic, chiral

DOI: 10.1002/elan.((will be filled in by the editorial staff))

1. Introduction

Solid–liquid interfaces play key roles in biology, sensing, separations, and energy storage-systems, e.g. batteries and supercapacitors.[2-18] The interface between a surface and aqueous solution is often described using the continuum model provided by the Poisson-Boltzmann equation[16, 17, 19-23] when considering biological or biosensing systems. In this model, ions are treated as point charges and the solvent is described as a homogeneous continuum. On the other hand, the interface between a surface and a non-aqueous solution – *where the classical model of the electrical double layer might not apply*[4,

[24, 25] [26-29] – is of importance in separation processes and energy-storage devices. Electrochemical platforms that rely on lithium salts in carbonate solvents are a preeminent example of the importance of interfaces in non-aqueous electrolyte systems.[30-32] Here, with the goal of developing a deeper understanding of non-aqueous interfaces, we probe propylene carbonate (PC) in the presence of a lithium salt ($LiClO_4$) at silica interfaces, using nonlinear optical spectroscopic, electrochemical, and electrokinetic measurements. We further consider the role of enantiomeric excess (i.e., the absolute difference between the mole fraction of each enantiomer) on the properties of PC at this interface.

In recent experiments, we showed that acetonitrile (MeCN) creates a spatially organized structure at silica surfaces that is preserved even at high concentrations of inorganic salts, including $LiClO_4$, $NaClO_4$, $LiBF_4$, and $LiPF_6$.[33, 34] The solvent arrangement is reminiscent of a supported lipid bilayer, such that the cyano groups of the first sublayer of MeCN molecules point toward the silica surface, whereas molecules in the second sublayer tend to have cyano groups pointing toward the bulk solution.[35] The methyl groups of the two sublayers are interdigitated in a hydrophobic region. This bilayer-like organization (described previously,[35] and referred to here as the "surface bilayer") is repeated with decreasing fidelity over a few nanometers into the solution. Through electrokinetic experiments, vibrational sum-frequency-generation (VSFG) spectroscopy, and molecular dynamics simulations, the solvent structure was found to direct the location of ions and to determine the effective potential of the interface.[33] At low concentrations of ions, the interface is negatively charged, due to the cyano groups that point into the bulk liquid. However, at a threshold concentration that depends on the identity of the salt, the interface acquires a positive effective potential. The presence of negative and positive potentials was detected by recording the direction of electroosmosis in single pores.[33, 36, 37] These results underscore the importance of the solvent in the electrochemical properties of a solid–liquid interface, and point to limitations in the ability of the classical electrical double layer model to describe interfaces involving some organic solvents.

Inspired by findings of spatial organization of MeCN and its role in the formation of the effective potential, we considered additional questions. First, is interfacial solvent organization sensitive to the enantiomeric excess of chiral solvent molecules? Second, if interfacial molecular structure is indeed affected by the enantiomeric excess of the solvent, can these differences influence the interfacial potential? To answer these questions, we chose PC as our model system. PC is a chiral solvent whose enantiomerically pure forms are readily available commercially. Our previous VSFG experiments with neat PC revealed that the arrangement of PC molecules on glass is indeed different for the racemic liquid and the enantiomerically pure liquid.[38] We also probed electrokinetic phenomena in pores in contact with $LiClO_4$ solutions in both types of PC, and concluded that the effective surface potential induced by racemic PC (which we henceforth denote as *rac*PC) is indeed higher than the potential induced by (*R*)-(+)-PC (which we henceforth denote (*R*)-PC).[38] These measurements, however, were not able to determine the magnitude of the potential, and moreover were recorded in salt-concentration gradients, which made interpretation of the potential as a function of salt concentration difficult.

In this manuscript we quantify the effective interfacial potential in two types of pores in contact with $LiClO_4$ solutions prepared in *rac*PC and (*R*)-PC. VSFG characterization [33, 38, 39] of a quartz–PC interface was performed over a wide range of $LiClO_4$ concentrations. These experiments reveal significant differences in the solid–liquid interfaces of *rac*PC versus (*R*)-PC solutions. The sign and magnitude of the interfacial potential were measured using glass nanopipettes with sub-100-nm diameters. The rectification properties in symmetric electrolyte concentrations[40-43] and the streaming current[19, 44] were measured in this system. These experiments reveal that glass pipettes in contact with *rac*PC solutions exhibit higher positive potential than do glass pipettes filled with (*R*)-PC solutions at the same $LiClO_4$ concentration. Finally, we present measurements that probe the presence of the effective surface potential in pores prepared in polyethylene terephthalate (PET) films.[45, 46] Similar to glass pipettes, the PET pores exhibit a higher interfacial potential when in contact with the solutions based on *rac*PC. Our work highlights the extreme sensitivity of the interfacial potential to the molecular organization of the solvent and underscores the need to develop a

deeper understanding of chiral electrokinetic phenomena.

2. Materials and Methods

2.1. Chemicals

$LiClO_4$ (≥99.99% battery grade, Sigma Aldrich) and KCl (≥99.0% Sigma-Aldrich) were used as received. Racemic PC (99.7% pure HPLC Grade, Sigma Aldrich), and (*R*)-(+)-propylene carbonate (purity >98%, TCI chemicals) were used in the experiments. Aqueous solutions were prepared with Milli-Q water (resistivity = 18.2 MΩ·cm at 25 ºC, Thermo Scientific) and filtered with a 0.20-µm PVDF nylon syringe filter (MicroLiter). We note that PC is only weakly hygroscopic,[47] and can gradually take up moisture if exposed to a humid atmosphere. For the single-pore and zeta-potential measurements, *rac*PC was dried over activated sieves in a glovebox under a nitrogen atmosphere, and (*R*)-PC was used as received. The (*R*)-PC and its solutions used for the experiments described here were exposed to the ambient atmosphere for a maximum of one hour, so we believe they are largely free of water. For the VSFG experiments, both *rac*PC and (*R*)-PC were used as received. The neat liquids and solutions were sealed in dried cuvettes as quickly as possible. We note that the VSFG spectra presented below rule out the presence of any significant amount of interfacial water. For the other experiments described here, no additional efforts were made to exclude adventitious water.

2.2. VSFG measurements

The laser source for our VSFG setup is a 1 kHz, Ti-sapphire, regenerative amplifier (Coherent Legend Elite), which generates 800-nm, 80-fs pulses, and has an average power of 3 W. The amplifier is seeded by a 76-MHz, Ti-sapphire oscillator (Coherent Mira) that is pumped with 5.2 W of the output of a continuous wave, 532-nm laser (Coherent Verdi-12) laser. The amplifier is pumped by a 1-kHz, Q-switched, frequency-doubled, Nd:YLF laser (Coherent Evolution). The amplifier output is directed through a 30/70 beam splitter, after which ~1 W of the output is sent to the mid-IR-generating path and the remaining 2 W to the probe path. The former path includes optical-parametric amplifier and noncollinear difference-frequency-generation modules (TOPAS, Light Conversion) that produce an IR beam with a bandwidth of 250 cm^{-1}, centered for the experiments reported here at 2945 cm^{-1}, with a maximum pulse energy of 15 mJ. The IR beam excites vibrations in the C–H stretching region of the spectrum.

The probe-beam portion of the amplifier output is spectrally narrowed using a 4*f* pulse stretcher and a slit, reducing the bandwidth to ~5 cm^{-1}, after which the pulse energy is ~15 mJ. The probe beam then traverses a delay line. The IR and probe beams meet at the sample in a counterpropagating geometry, with incident angles of 61° and −58° from the surface normal, respectively. The signal is generated at an angle of −32.8° and is collected using a spectrometer (ActonSP300i) with a thermoelectrically cooled CCD camera (Spec-10:100, Roper Scientific). The experiments were performed in the *SSP* polarization configuration, with the polarizations listed in the order of the signal, probe, and IR. *P* denotes polarization in the plane of incidence and reflection, such that there is a projection of the polarization along the surface normal. *S* denotes polarization perpendicular to the plane of incidence and reflection, and therefore perpendicular to the surface normal. Eight 120-s scans were performed for each sample. The individual spectra were normalized to the nonresonant SFG signal from a gold substrate. A polystyrene film placed in the path of the IR beam while measuring the gold SFG signal was used to calibrate the frequency of the signal, using four of the polystyrene absorption peaks.

The cuvettes used for the VSFG studies were composed of IR-grade quartz (FireflySci). Before use, the cuvettes were rinsed sequentially with contaminant-free methanol, de-ionized water, and then acetone. The cuvettes were then oven-dried and placed in an oxygen plasma cleaner (Herrick) for 3 min.

2.3. Preparation of quartz nanopipettes

Quartz capillaries (Q100-70-7.5, Sutter Instrument) were pulled with a CO_2-laser puller (P-2000, Sutter Instrument) to fabricate single-barrel nanopipettes. A typical set of program parameters used was: Heat, 640; Velocity, 3; Filament, 40; Delay time, 180; and Pull, 155. The pipettes were characterized by

scanning electron microscopy (FEI Quanta-FEG), which revealed a typical inner diameter of 72 ± 2 nm and an outer diameter of 104 ± 5 nm, as shown in Figure S1.

2.4. Preparation of pores in poly(ethylene) terephthalate (PET) films.

Single pores were fabricated in PET membranes using the track-etching technique.[45] This method involves irradiation of a 3-cm-diameter, 12-µm-thick PET film using single, heavy, energetic (11.4 MeV/µ) ions of Xe, Au, or U (UNILAC, Universal Linear Accelerator at the Institute for Heavy Ions Research, Darmstadt, Germany), leading to the formation of a single damage track. A 100-µm-diameter metal mask located in front of the film, combined with adjustment of the ion beam to allow only one heavy ion to pass through the mask's aperture, leads to the creation of a single pore. The ion beam is shut down when an ion detector located on the opposite side of the film registers an event.[48] The films are then exposed to 365-nm light for 1 h on each side using a 115-V, UVGL-25 compact UV lamp (UVP, LLC), to ensure a more homogenous etching along the heavy-ion track.[49] Following the UV treatment, the films are subjected to wet chemical etching in 2 M NaOH at 60 °C.[46] PET pores prepared by the track-etching method under the described conditions have been shown to exhibit symmetric, cylindrical shape, with an average pore diameter that increases linearly with chemical-etching time.[46, 50] The diameters of single PET pores were determined electrochemically by measuring the pore resistance in a 1 M aqueous KCl solution, as reported previously.[37] These high-ionic-strength conditions assure that the pore volume is filled with the bulk solution and that surface-charge effects are screened.

2.5. Electrokinetic and streaming-current measurements

2.5.1. Quartz nanopipettes

For nanopipette experiments, a two-electrode system was used to perform current–voltage (I–V) measurements with a picoammeter–voltage source (Keithley 6487, Keithley Instruments). A back-inserted Ag/AgCl wire inside the nanopipette served as the working electrode, and an Ag/AgCl pellet was placed in the bath solution which served as the reference electrode. The transmembrane potential was ramped from -3 V to 3 V at 0.2 V/s. For streaming-current measurements in nanopipettes, a Ag/AgCl wire was back-inserted into the pipette, and a second Ag/AgCl electrode was placed in the bath solution. Current–time traces were measured with the headstage of an Axopatch 200b current amplifier (Molecular Devices) with a gain of 1 mV/1pA and with a low-pass filter set to 1 kHz (-3 dB, 4 pole Bessel). Current was recorded at a sampling frequency of 50 – 100 kHz, using a low-noise data-acquisition system and pClamp 10.6 software (Axon Digidata 1440A, Molecular Devices). Pressure application through the side arm of the electrode holder (Warner Instruments) was performed with a high-speed pressure clamp (ALA Scientific) and was controlled through a pClamp protocol. The pressure protocol stepped in increments of 50 mmHg that were each held for a duration of 8 s, then returned to 0 mmHg after each step, before proceeding to the next increment. The current recorded during the 140 ms prior to each pressure step (i.e., at 0 mmHg) was averaged and used as the initial current value (I_i). During a pressure step, the ion current was measured for a duration of 1 s, and an averaged value was calculated as the streaming-current (I_{str}) value for each pressure. The change in the measured current, $\Delta I = I_{str} - I_i$, was determined for each pressure step.

2.5.2. Single pores in PET

Electrokinetic measurements with polymer membranes were performed using a home-made conductivity cell in which the single-pore membrane was mounted between two chambers filled with different concentrations of $LiClO_4$ in PC; we denote these concentrations c_{high} and c_{low}. I-V curves were recorded with a Keithley 6487 picoammeter/voltage source (Keithley Instruments), with pellet Ag/AgCl electrodes serving as the working and reference electrodes in their respective chambers of the solution. The instrument was controlled using software written in LabVIEW (National Instruments). The voltage was varied between -2 V and +2 V in 0.1 V steps. Each PET membrane was exposed to 0.1 mM/1 mM, 0.5 mM/5 mM, 1 mM/10 mM, and 10 mM/100 mM concentration gradients of $LiClO_4$ prepared in *rac*PC or (*R*)-PC. Before switching salt concentrations, both chambers of the

conductivity cell were rinsed thoroughly in neat solvent. For consistency, the ground electrode was always placed in the lower-concentration solution, and the working electrode was always placed in the higher-concentration solution. All I-V curves reflect average values and standard deviations from at least three forward and three reverse scans.

Streaming-current measurements were performed on PET pores using a home-made conductivity cell, modified with a custom hydrostatic-pressure setup. The single-pore membrane was mounted between two chambers containing an electrolyte solution with the same concentration. One side of the membrane was exposed to atmospheric pressure and contained a pellet Ag/AgCl electrode submerged in the solution; this electrode served as the reference electrode. The other side of the membrane was airtight, and hydrostatic pressure was applied by manually varying the height of the liquid column via a system of plastic tubing. This side of the membrane also included a pellet Ag/AgCl electrode, which served as the working electrode. An Axon Instruments Axopatch 200B integrated patch clamp combined with a 1322A Digidata acquisition system (Molecular Devices) was used to record I_{str}. The hardware was operated in the whole-cell model ($\beta = 1$), employing a 1 kHz, low-pass Bessel filter, and I_{str} was sampled at a frequency of 1 kHz. The ion current at each applied pressure was measured for 15 s, and the values were subsequently averaged over time.

In both the membrane and pipette measurements, ambient electrical noise was minimized by use of a Faraday cage (Warner Instruments for the membranes and a home-built cage for the pipettes). Vibrational noise was reduced with a vibration-cancellation table (TMC for the membranes and Herzan for the pipettes). The ion current was recorded as a time series and was analyzed using Clampfit (Molecular Devices) and Igor Pro (Wavemetrics, Lake Oswego, OR, USA).

3. Results and Discussion

3.1. VSFG characterization of the solid–liquid interfaces of quartz and *rac*PC and (*R*)-PC solutions of $LiClO_4$

VSFG spectroscopy is especially well-suited to probe solid–liquid interfaces, because this technique is sensitive to molecular arrangements in regions in which centrosymmetry is broken.[51, 52] We used this approach previously to probe the molecular structure of an interface created by quartz in contact with $LiClO_4$ solutions in MeCN.[33, 34] We found that the lipid-bilayer-like organization of MeCN at this interface is largely preserved in 1 M $LiClO_4$.[33] Due to the spatial organization of MeCN at this interface, lithium ions were found first to accumulate on the surface of the second sublayer to neutralize the partial negative charge on the nitrogen atoms in the cyano groups. Only at a threshold concentration of ~1 mM

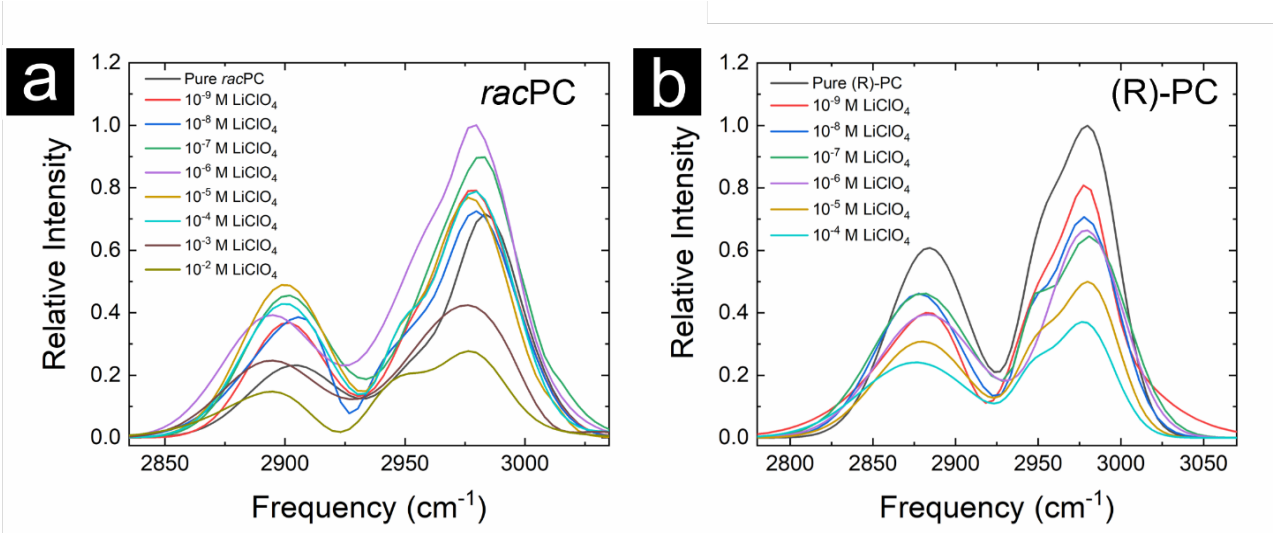

Figure 1. Gaussian fits to VSFG spectra for $LiClO_4$ prepared in (a) *rac*PC, and (b) (*R*)-PC. The raw spectra are presented in Figure S2. The spectra were normalized with respect to the highest signal recorded at 10^{-6} M $LiClO_4$ in (a) and with respect to the neat (*R*)-PC signal in (b).

$LiClO_4$ could anions begin to enter the bilayer, allowing lithium to accumulate at the silica and outer bilayer surfaces to render this interface effectively positively charged.[33]

PC also has a large dipole moment (~4.9 D), and the partial negative charge on the carbonyl oxygen can attract Li^+ ions to fulfill electroneutrality if PC molecules create organized bilayers. Based on the VSFG data for neat *rac*PC,[38] as well as on molecular dynamics simulations of the organization of *rac*PC on a positively-biased graphite electrode,[53] this solvent is expected to create a structure on silica that is similar to those observed for MeCN[33, 35, 54] and propionitrile.[27, 55] We hypothesized that, as is the case for MeCN, the interfacial organization of PC molecules determines the ionic distribution and the effective potential. Here we use VSFG to probe the solvent organization as a function of electrolyte concentration at a quartz surface in contact with $LiClO_4$ solutions in both types of PC.

Figure 1 compares VSFG spectra recorded for $LiClO_4$ solutions in *rac*PC and (*R*)-PC. Due to the limited signal-to-noise ratio in the (*R*)-PC solutions, we show Gaussian-fitted spectra of both types of solutions to facilitate comparison; the raw data are presented in Figure S2. Reliable fitting was not possible at the highest concentrations of $LiClO_4$; thus we show fitted spectra only up to 10 mM and 0.1 mM $LiClO_4$ for *rac*PC and (*R*)-PC, respectively.

The two broad peaks observed in the VSFG spectra in **Figure 1** are attributed to symmetric C-H stretches of the methyl, methylene, and methine groups (~2920 cm^{-1}) and asymmetric C-H stretches of the methyl and methylene groups (~2980 cm^{-1}).[38] The concentration-dependent behavior of the spectra for the racemic solutions are similar to those for MeCN,[33] with the asymmetric stretch intensity increasing up to a concentration of 10^{-6} M $LiClO_4$ and the symmetric stretch intensity increasing up to a concentration of 10^{-5} M of $LiClO_4$ before decreasing at higher concentrations. These data indicate that the lipid-bilayer-like organization of *rac*PC causes cations to partition to the outside of the bilayer until the effective charge of the carbonyl oxygens has been neutralized. The partial negative charges on the carbonyl groups act as an electrostatic barrier that prevents anions from entering the bilayer, and the bilayer itself is compact enough to make it energetically unfavorable for cations to partition to the silica surface until anions can also enter the bilayer, which provides sufficient structure disruption to allow the cations to pass through, in analogy to what has been observed previously for MeCN.[34] The increase in the VSFG intensity at low concentrations of $LiClO_4$ indicates that the presence of Li^+ at the outside of the bilayer changes the orientational distribution of the *rac*PC molecules in the second sublayer, which is consistent with the known propensity for lithium ions to associate with, and organize, the carbonyls groups of neighboring PC molecules.[56, 57] Raman non-coincidence effect studies have shown that the carbonyl groups of PC molecules tend to dipole pair in the bulk liquid,[58] and it might therefore be expected that the carbonyl groups of PC molecules in the second sublayer dipole pair with those of adjacent molecules in the bulk liquid. The presence of cations should disrupt such ordering. Together these effects likely account for the change in preferred orientation that leads to the increase in the VSFG intensity.

Once the outside of the surface bilayer of *rac*PC has been neutralized, it becomes energetically favorable for cations to partition to the surface and for anions to partition into the bilayer. Accordingly, the VSFG intensity begins to decrease, reaching half of its peak value at an electrolyte concentration of 10^{-3} M. In our previous studies of electrolyte solutions in MeCN,[33] we noted that perchlorate is a large anion with delocalized charge, and so can be considered to be relatively hydrophobic, although some hydrogen bonding from surface silanol groups was also observed. However, the carbonyl carbon in PC is bonded to three different electron-withdrawing atoms, and so carries nearly a full positive charge.[59] We therefore expect that there will be strong interactions between the carbonyl carbons in each sublayer and any perchlorate ions that are inside of the bilayer. These interactions will have a significant impact on the organization of the interfacial solvent, leading to the observed decrease in the VFSG intensity at higher concentrations of $LiClO_4$. Taken together, our observations suggest that $LiClO_4$ in *rac*PC can induce an effective positive charge at a silica interface at significantly lower concentrations than observed in solutions of $LiClO_4$ in MeCN.

The VSFG spectra for $LiClO_4$ in (*R*)-PC solutions differ markedly from those recorded in *rac*PC

solutions (**Figure 1b**). In (*R*)-PC, the signal decreases monotonically with increasing concentration over the entire examined range of $LiClO_4$ concentrations examined, reaching half of the peak value at 10^{-5} M. To rationalize this result, we note that manufacturer's reported data suggest the density of bulk (*R*)-PC at 25 °C (1.189 g/mL) is about 1 % less than that of *rac*PC (1.204 g/mL).[60, 61] This difference can be a manifestation of possible packing constraints imposed on (*R*)-PC by only having a single enantiomer. The free volume in bulk (*R*)-PC could therefore be substantially larger than that in bulk *rac*PC. These effects should be recapitulated in the surface bilayer of (*R*)-PC. Although the organization of the first sublayer may be determined largely by the surface silanol groups with which the (*R*)-PC molecules hydrogen bond, the second sublayer is expected to be considerably more disordered than in the case of *rac*PC, explaining why the VSFG signal for neat (*R*)-PC at the silica interface is substantially larger than that for *rac*PC.[38]

We hypothesize that a larger free volume in the surface bilayer of (*R*)-PC allows cations to partition to the silica surface even at low concentrations of $LiClO_4$, influencing the organization of the first sublayer, and causing the VSFG signal to drop. The perchlorate anions are considerably larger than the lithium cations, but likely can also enter the bilayer even at low concentrations, as the electrostatic barrier of the second sublayer will be weaker than in *rac*PC. The presence of lithium ions at the silica surface will also create a driving force for anions to enter the bilayer.

VSFG measurements revealed that molecular organization at the quartz–PC interface is sensitive to whether the solvent is racemic or enantiomerically pure. Below, we use electrochemical approaches to probe the presence and magnitude of the interfacial surface potential as a function of $LiClO_4$ concentration in both types of PC. We first describe experiments using quartz pipettes, in which the surface chemistry at the walls of the pipette is chemically similar to that of the quartz surfaces used for spectroscopic experiments.

3.2. Electrochemical properties of nanopipettes in $LiClO_4$ solutions in *rac*PC and (*R*)-PC

Quartz pipettes pulled to small diameters provide a versatile platform for probing interfacial charge. The asymmetric conical structure of the pipette tip, combined with a relatively small opening diameter (<100 nm), results in transport properties that are dominated by the interplay among the glass surface, the geometry of the pipette, and the electrolyte solution. The asymmetry of the shape of the pipette, combined with the presence of the finite surface potential, results in asymmetry in transport of ions at the pipette opening. These effects have been widely exploited in sensing and imaging experiments.[62-65] Here, we use nanopipettes to measure ion currents induced by applied potentials and pressures.

For the experiments described here, a symmetric ion concentration was employed on each side of the nanopipette, providing a direct measurement of ion transport, analogous to typical I-V measurements in nanopores. The combination of the conical geometry and the presence of a surface charge results in a voltage-polarity-dependent number of charge carriers in the pore, and a voltage-polarity-dependent magnitude of the ion current, recorded as ion-current rectification.[40, 41, 65-68] The measured I-V curves are therefore characterized by a ratio of currents recorded at the same magnitudes of voltage but opposite polarities. In our electrode configuration, pipettes in contact with aqueous salt solutions rectify such that negative currents are larger than positive currents. This behavior is expected, based on the presence of silanol groups on the pipette walls. On the other hand, if a pipette is chemically modified to become positively charged, its I–V curves will be inverted, such that currents at positive voltages will be higher.[42, 65] Numerically, this behavior can be quantified via the absolute value of the ratio of the ion currents at two equivalent applied positive and negative potentials (here with a magnitude of 3 V), which is referred to as the ion–current rectification ratio (ICRR):[69-72]

$$ICRR = \left|\frac{I_+(+3V)}{I_-(-3V)}\right| \quad \textbf{Equation 1}$$

For the experiments shown here, ICRR > 1 (ICRR < 1) indicates presence of positive (negative) surface charges.

The I-V responses of nanopipettes in *rac*PC and (*R*)-PC as a function of $LiClO_4$ concentration are shown in **Figure 2(a-c)**, and the calculated ICRR at ±3 V is

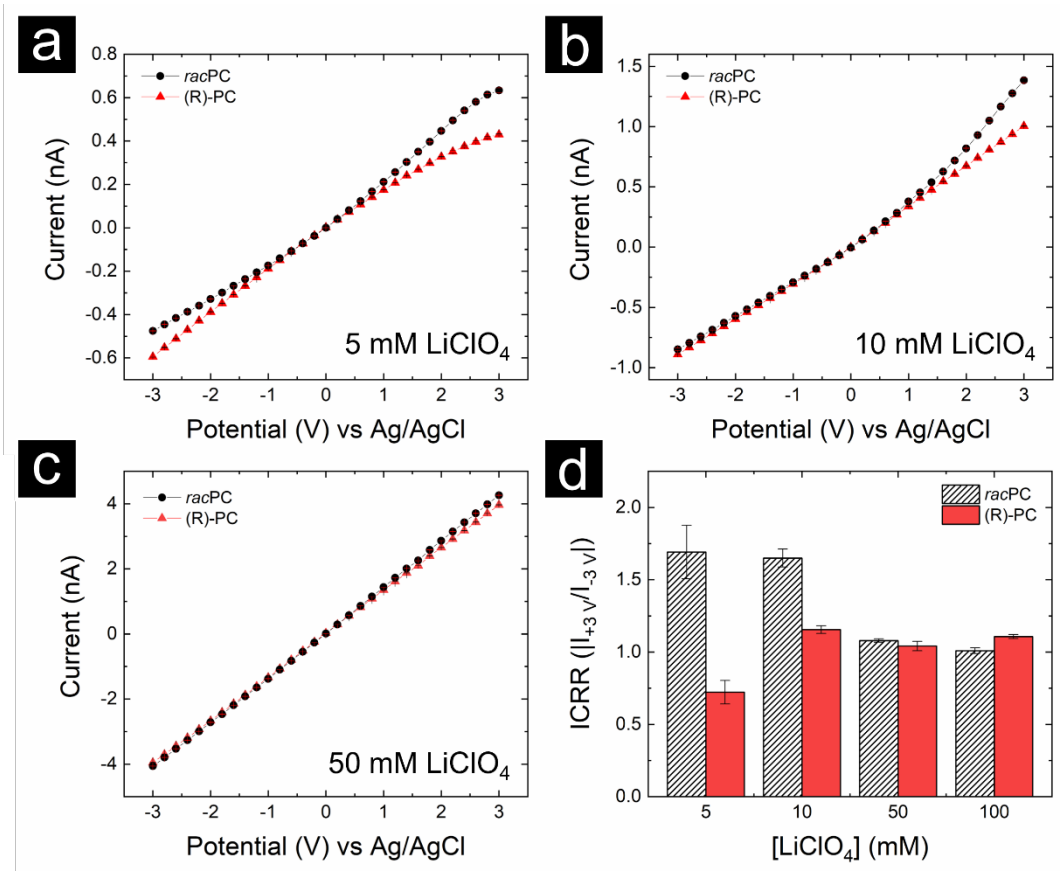

Figure 2. I-V response of quartz nanopipettes filled with *rac*PC and (*R*)-PC with $LiClO_4$ concentrations of (a) 5 mM, (b) 10 mM, and (c) 50 mM. Note the identical currents recorded at low voltages for both types of solutions at each $LiClO_4$ concentration, in agreement with nearly identical ionic conductivities of racemic and enantiomeric PC solutions.[1] For a-c, error bars are the standard error of the mean from at least 3 replicant measurements. (d) Calculated ion–current rectification ratio at ±3 V for different electrolyte concentrations. Error bars are standard error of the mean for at least 4 separate measurements.

shown in **Figure 2d**. To minimize pipette-to-pipette variation, a single capillary was pulled into two nominally identical pipettes, which we refer to as "sister" pipettes. One sister pipette was filled with a $LiClO_4$ solution in *rac*PC, and the second sister pipette was filled with a $LiClO_4$ solution of identical concentration in (*R*)-PC. The nominal inner diameter of the pipettes used to collect data was 72 ± 2 nm, as characterized by SEM. For the lowest electrolyte concentration (5 mM), the results for *rac*PC and (*R*)-PC differed, with *rac*PC exhibiting an ICRR > 1 and (*R*)-PC exhibiting an ICRR < 1, which suggests a nominal positive charge in *rac*PC and a nominal negative charge in (*R*)-PC. At a 10 mM electrolyte concentration, both *rac*PC and (*R*)-PC exhibit ICRR > 1, suggesting a nominal positive charge. We note that the pipettes did not undergo any chemical modification, implying that the positive charge results from the arrangement of solvent molecules and ions at the interface. The magnitude of the ICRR in 10 mM $LiClO_4$ is, however, significantly higher in *rac*PC (~1.7) than in (*R*)-PC (~1.2). These observations are consistent with our earlier findings in polymer and silicon nitride pores, in which a lower magnitude of the effective surface potential in (*R*)-PC solutions was observed at similar concentrations.[38] Finally, for even higher concentrations (50 and 100 mM), the ICRR is close to 1 for both types of PC, suggesting that the pipettes either become near neutral, or that the surface charges are screened by the high salt concentration. Linear I-V curves for conically-shaped and charged pores are indeed recorded at concentrations above a threshold salt concentration at which the ion concentrations in the pores are no longer regulated by the presence of a surface potential.[40, 73] In such a case, the lack of rectification is not indicative of a lack of finite surface charge, but rather points to effective screening of the

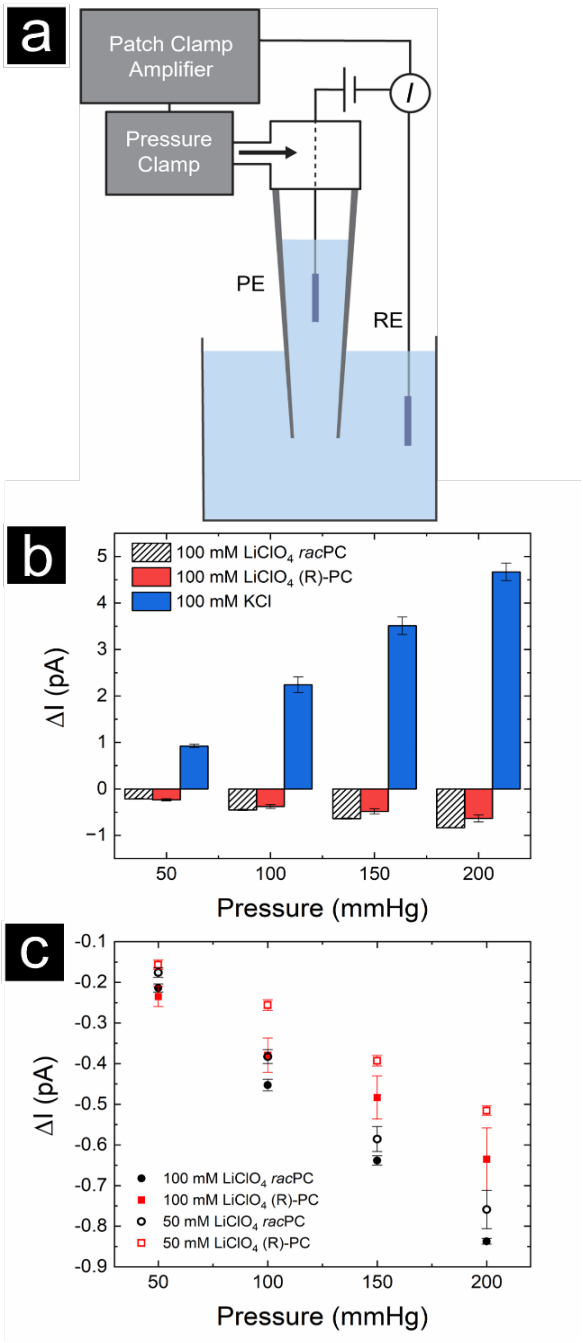

Figure 3. (a) Schematic for streaming-current measurements in quartz nanopipettes. (b) The streaming current (ΔI) as a function of applied pressure for pipettes filled with *rac*PC and (*R*)-PC with 100 mM $LiClO_4$, and with 100 mM KCl in water. (c) The streaming current as a function of applied pressure for 50 mM and 100 mM $LiClO_4$ solutions. For (b) and (c), error bars are the standard error of the mean for 3 separate measurements.

charges by ions in the solution. The results shown here are in qualitative agreement with results from multiple sets of sister pipettes tested.

To probe the presence and magnitude of the surface charge at the higher concentrations of 50 mM and 100 mM, we employed the electrokinetic approach of measuring the streaming current, which is known to be dependent on the zeta potential at the surface.[19] The zeta potential is the potential at a shear plane that is located some distance from the surface, and is often assumed to be the potential at the plane of the Stern layer. In the case of solid–liquid interfaces with a layered solvent, we expect that the shear plane will be positioned beyond the first bilayer. The streaming-current measurements entail placing a pipette in contact with the same solution on both sides, setting the transmembrane potential to 0 V, and recording ion current upon gradual increments of the pressure difference across the pipette. The measured streaming current is carried by the counterions at the interface. The streaming current is positive (negative) when the interface has an effective negative (positive) potential.[44] The streaming current is dependent on the zeta potential of the interface, providing a direct probe of the magnitude and sign of the zeta potential.

Streaming-current measurements for sister pipettes in *rac*PC and (*R*)-PC were recorded for applied pressures in the range of 0-200 mmHg, with a patch-clamp configuration such as is typically used for patching cell membranes (**Figure 3a**). In these measurements, differences between the current at zero pressure and at applied pressures (streaming currents) were at the limit of instrumental noise, which only allowed for recording of the changes in current as a function of pressure for 50 mM and 100 mM solutions of $LiClO_4$.

Streaming-current measurements in a quartz nanopipette filled with 100 mM KCl are shown in **Figure 3b** for reference. Glass surfaces are known to have a net negative charge at pH > 3, resulting in a positive streaming current, in agreement with previous observations.[74]

For *rac*PC and (*R*)-PC solutions of $LiClO_4$, consistent trends are observed for each condition. In accordance with expectation, over the range investigated, the streaming current increases as a function of the applied pressure for both solutions in a monotonic manner. The streaming currents for the 50 mM and

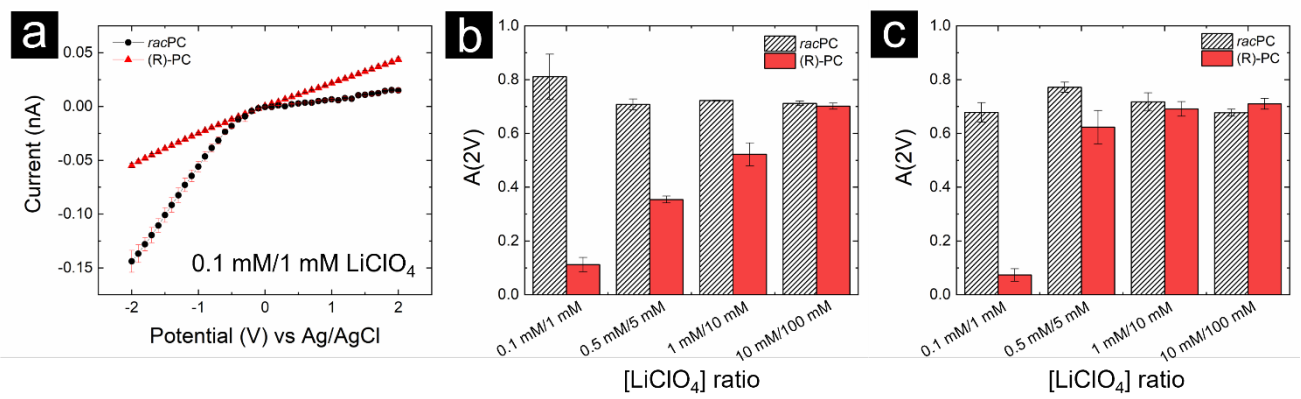

Figure 4. Electrochemical data for single PET pores. (a) I–V curves for a 390-nm-diameter pore when in contact with a 0.1 mM/1 mM concentration gradient of $LiClO_4$ prepared using either *rac*PC or (*R*)-PC. The error bars represent standard deviation from 3 replicant measurements. (b) Bar graph summarizing the ion-current anisotropy, *A*(2V), data for a range of concentration gradients. The error bars are calculated from propagation of error from Eqn. 2. (c) Bar graph summarizing *A*(2V) data for a single, 450-nm-diameter PET pore.

100 mM solutions are negative, providing evidence that the pipettes have an effective positive surface charge at higher electrolyte concentrations. The streaming current is slightly larger for the 100 mM concentration than for the 50 mM concentration, suggesting that the zeta potential in the higher concentration might be higher. Finally, *rac*PC exhibits higher negative streaming current values than does (*R*)-PC.

To calculate the magnitude of the zeta potential from streaming currents in glass pipettes, we would need to model pressure-driven flow in pipettes together with local ionic concentrations at the solid–liquid interface.

A simple approach to estimating zeta potential in PC solutions utilizes literature values of the zeta potential of glass in aqueous solutions, which is equal to -30 mV in 100 mM KCl.[75, 76] To use the magnitude of the zeta potential in 100 mM KCl to estimate the magnitude of zeta potential in 100 mM monovalent salt in PC, we first note that the velocity of ions driven by a pressure gradient is inversely proportional to the solution's dynamic viscosity. Consequently, we expect the streaming current to be inversely proportional to the value of dynamic viscosity as well. Furthermore, the streaming current is proportional to the relative permittivity of the solvent (see Eqn. 3 below). Streaming current is known to be higher for pores with a higher zeta potential. Because the ratio of the dynamic viscosity[77] to the permittivity of PC (2.5 mPa·s / 65) is ~3.4 times higher than that of water (0.89 mPa·s / 78) and the streaming current in water is ~5 times higher than in *rac*PC (Figure 3B), we conclude that the zeta potential in PC is lower than 30 mV. Assuming, further, that the streaming current in a pipette with a 72-nm inner opening radius is directly proportional to the zeta potential. and using the calculated ratio of 3.4, we estimate the zeta potential in 100 mM $LiClO_4$ in *rac*PC to be ~(3.4/5)·30 mV ~20 mV. Because the streaming current in *rac*PC is ~25% higher than that in (*R*)-PC (Figure 3B, C), the estimated zeta potential in (*R*)-PC is ~16 mV.

These electrokinetic measurements complement conclusions made based on I–V curves. In particular, the effective surface charge of glass pipettes in contact with 50 mM and 100 mM $LiClO_4$ solutions remains positive in both types of PC solutions. However, the magnitude of the surface charge is higher in *rac*PC than in (*R*)-PC. The measurements also allow us to conclude that the differences in the molecular arrangement at the interface in *rac*PC and (*R*)-PC observed through I–V curves at low salt concentrations (Figure 3) are preserved at high salt concentrations.

The measurements with quartz pipettes are also in agreement with the VSFG spectra of a quartz surface in contact with PC electrolyte solutions (**Figure 1**). The *rac*PC can create a more organized layered structure at the interface, changing the ability of cations and anions to enter the surface bilayer. Accumulation of anions within the bilayer, as indicated by the VSFG spectra, leads to a local

accumulation of lithium ions and the formation of an effective positive surface charge in all probed $LiClO_4$ concentrations in *rac*PC. The layered structure for (*R*)-PC-based solutions is less organized and has greater free volume, such that the accumulation of lithium ions, and the resulting positive charge, are weaker.

3.3. Single PET pores exhibit an effective surface potential that is dependent on the enantiomeric excess of PC

The enantiomeric-excess-dependent interfacial potential was also tested in single pores in a PET film exposed to $LiClO_4$ solutions in *rac*PC and (*R*)-PC. PET pores prepared by the track-etching technique contain a high density of carboxylic acid groups.[78, 79] We hypothesized that the carbonyl groups in PC will accept hydrogen bonds from the carboxylic acid groups, similar to what is observed for silanol groups in silica.[38] Consequently, PC would also be expected to create a layered structure near a PET surface.

To determine the presence and polarity (positive or negative) of interfacial potential on PET pores, we used a different method than the one applied for the glass pipettes. The approach used is applicable to pores of any diameter and enables detection of surface charge even in large pores and at high electrolyte concentrations. Instead of conically shaped nanopores, we prepared cylindrically shaped pores with an opening of a few hundred nm in diameter.[36, 37] Such single-pore membranes were placed between two electrolyte solutions with concentrations c_{low} and c_{high}. This situation naturally leads to ion-current rectification when the interface exhibits a non-zero potential. By construction, with the ground electrode placed in the chamber with c_{low}, it can be deduced that when the interface carries an effective negative potential, the direction of electroosmosis will be determined by the cations. For example, for positive applied voltages, the cations will electroosmotically drag the solution with c_{high} into the pore, and for negative applied voltages, the pore will be filled with the solution with c_{low}. Therefore, a pore with a negative surface potential will exhibit asymmetric I-V behavior, such that $|I(+V)| > |I(-V)|$. A pore with a positive surface potential, on the other hand, will lead to asymmetric I–V curves with $|I(+V)| < |I(-V)|$. A complete, in-depth explanation of the influence of electroosmosis in the electrical setup has been given previously.[38] The positive/negative polarity of the surface potential of the pores can thus be easily deduced from the characterization of I–V curves recorded under an electrolyte-concentration gradient.

All I–V curves were characterized using the ion current anisotropy, $A(V)$, defined previously as[33, 38]:

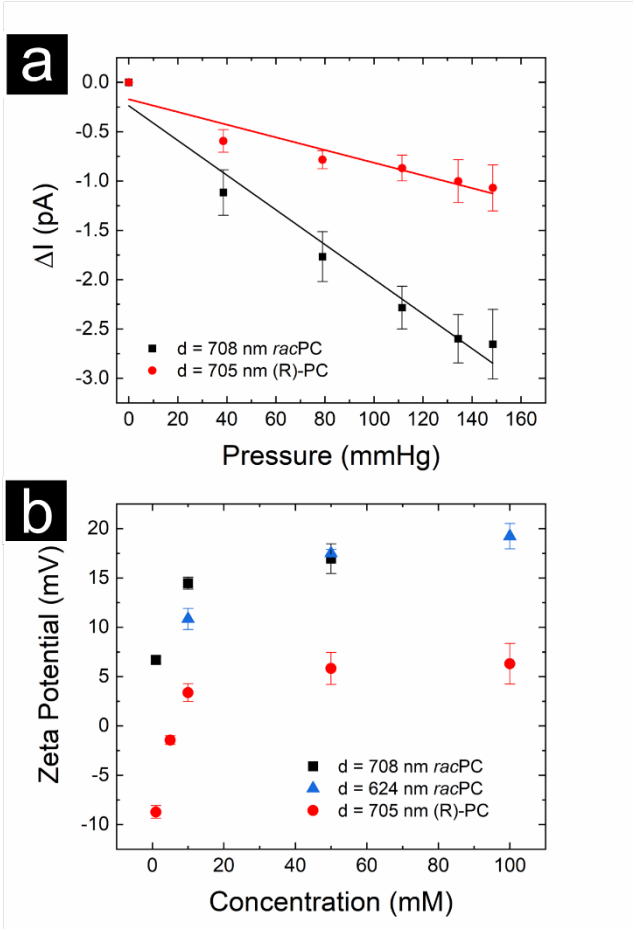

Figure 5. (a) Streaming current through single PET pores with an opening diameter of ~700 nm recorded in 50 mM $LiClO_4$ in *rac*PC and (*R*)-PC. Error bars are standard deviation of streaming current averages over 15 s at each pressure. (b) Calculated zeta potentials as a function of the concentration of $LiClO_4$. Data for three single PET pores of different diameters (*d*) are reported. Error bars are determined by propagation of error from calculation of zeta potential (Eqn. 3). Error originates from measured slope dI/dP and measured cross-sectional area.

$$A(\mathrm{V}) = \frac{I(-V)+I(V)}{I(-V)-I(V)}$$ **Equation 2**

By the defined convention, a positive effective surface potential leads to a positive value of A(V), and vice versa. The magnitude of A(V) is an indirect measure of the magnitude of the surface potential, i.e. pores with larger surface potentials produce I–V curves that are more asymmetric, because pores with a lower (higher) interfacial potential will be filled less (more) completely with a solution of either side, leading to lower (higher) A(V). Note that the origin of rectification and a non-zero ion-current anisotropy value here is different from the origin of the ICRR observed in nanopipettes (**Figure 2**).

Figure 4 a,b shows I–V curves and A(2V) for a single PET pore with a diameter of 390 nm. These measurements were performed with $LiClO_4$ solutions prepared using either *rac*PC or (*R*)-PC. Under the lowest concentration gradient, 0.1 mM/1 mM, the I–V curve for the *rac*PC solution suggested that the pore exhibits a strong effective positive surface potential. However, when the same concentration gradient was used with (*R*)-PC, the I–V curves were effectively linear, indicating that the effective surface potential was close to zero. As the concentrations on both sides of the pore were increased, the pore began to rectify in the same direction in both *rac*PC and (*R*)-PC, up to the largest concentration gradient studied, for which the I–V curves and values of A(2V) for both types of solutions became identical. These results agree well with our previous work.[38] Data for another, independently prepared pore, are shown in **Figure 4c**; this pore had transport properties in *rac*PC and (*R*)-PC that were qualitatively similar to the pore in **Figure 4 a,b**.

Although the ion-current anisotropy allows us to draw comparisons of effective surface potentials measured under different conditions, we cannot directly relate A(V) to the magnitude of the effective surface potential. To quantify the surface potential, we again turn to the electrokinetic method of measuring the zeta potential through recording streaming current.[19, 80-82] Here, we use the relationship derived from combining the charge-density distribution in the diffuse layer and the pressure-driven flow of the electrolyte in a microfluidic system. In our measurements and analysis, we use a relationship that was analytically determined for a cylindrical capillary using the Poisson-Boltzmann and Navier-Stokes equations.[19, 80] In this case, I_{str}, is proportional to the applied pressure, P, with a proportionality constant that depends on the zeta potential, ζ:

$$I_{str} = -\frac{A\,\varepsilon_r\varepsilon_0}{\eta}\,\frac{P}{L}\,\zeta$$. **Equation 3**

This formula is valid for cases in which the electrical double layer, or, more generally, the interfacial region with modified concentrations, is thin compared to the pore radius, which holds for our ~400-nm-diameter pores. Because we measured the streaming current as the pressure was slowly varied, we can use the slope of a linear fit to the current vs. pressure curve, $\Delta I_{str}/\Delta P$, when calculating ζ for each ionic concentration. A representative current vs. pressure curve, including a linear fit for extracting $\Delta I_{str}/\Delta P$, for 50 mM $LiClO_4$ in *rac*PC and (*R*)-PC is shown in **Figure 5a**. This approach has the advantage of being insensitive to a current offset and being more precise than a measurement using only a single current value. The diameter of each pore was measured electrochemically and used to calculate the cross-sectional pore area A. The channel length (L = 12 μm), as reported by the manufacturer, and tabulated values of the permittivity (ε_r = 65 at 25 °C, $\varepsilon_0 = 8.85 \times 10^{-12}$ F/m) and the dynamic viscosity (η = 2.5 mPa·s at 25 °C)[77] were used to calculate values of ζ .

Figure 5 shows representative streaming currents and the cumulative zeta-potential measurements for three different, single, PET pores at different concentrations of $LiClO_4$ in *rac*PC and (*R*)-PC. When the membranes were in contact with solutions prepared in *rac*PC, the zeta potential at all concentrations was positive. When a membrane was in contact with solutions prepared in (*R*)-PC, the zeta potential for concentrations greater than 5 mM was also positive and followed a similar dependence on ionic concentration to that for *rac*PC, but with a significantly lower magnitude. This behavior agrees with our electroosmosis results (**Figure 4**). Specifically, at the lowest concentration gradient studied, 0.1 mM/1 mM $LiClO_4$, the magnitude of A(2V) was nearly an order of magnitude smaller for (*R*)-PC than for *rac*PC. We also note that there is a visible dependence of the zeta potential on ionic concentration for both types of PC, which was not previously detected by our electroosmosis technique.

In particular, at 5 mM $LiClO_4$, (*R*)-PC has a zeta potential that is close to zero, and at 1 mM $LiClO_4$ the zeta potential is negative.

We return to our VSFG results (**Figure 1**) to gain further insights into the origin of the electrolyte-concentration-dependent zeta potential in both types of PC. We hypothesize that PC molecules create organized bilayers, similar to what has been observed for MeCN, and that the negative charge on the carbonyl oxygen creates an inherently negative effective surface charge in the neat solvent.[33, 38] Our VSFG data indicate that at low and moderate concentrations of $LiClO_4$ in *rac*PC, cations can partition to the exterior of the bilayer and neutralize the partial negative charges on the carbonyl oxygens in the second sublayer. At higher concentrations, the interface becomes positively charged due to anions partitioning into the bilayer and lithium ions accumulating at the exterior of the bilayer and at the silica surfaces. The zeta-potential measurements for *rac*PC in **Figure 5** were obtained at concentrations well above the regime in which the VSFG data indicate that neutralization is achieved, and so the zeta potential is positive. We expect that if we were able to measure the zeta potential at a low enough concentration of $LiClO_4$ in *rac*PC, we would observe negative values.

Our VSFG results suggest that the surface bilayer in (*R*)-PC can be porous to ions even at the lowest concentrations measured, likely due to a larger free volume induced by packing constraints. Accordingly, ions can partition into the bilayer even at concentrations well below that at which the charge on the exterior of the bilayer has been neutralized. The ability of anions to partition into the bilayer even at low electrolyte concentrations allows the effective surface charge to remain negative up to a considerably higher electrolyte concentration than for *rac*PC. The zeta-potential measurements for (*R*)-PC indicate that the negative surface charge persists up to a $LiClO_4$ concentration of approximately 5 mM.

The electrochemical properties of PC solutions in PET pores, as studied using electroosmosis and ion-concentration gradients, as well as pressure differences and symmetric salt conditions, point to the same conclusion: the effective surface potential is dependent on whether *rac*PC or (*R*)-PC is used. There are, however, visible differences in the behavior of PC in PET pores probed with the two methods. Notably, at small salt concentrations, the zeta potential in (*R*)-PC is negative (Figure 5), in contrast to what is seen with the electroosmosis method (Figure 4), in which the parameter $A(2V)$ was positive in all conditions. Additionally, there is a significant difference in the magnitude of the positive zeta potential between *rac*PC and (*R*)-PC, which is not seen in the higher concentrations with the electroosmosis method. We propose that the differences in the results between these approaches stem from the presence of salt-concentration gradient in the EOF approach and symmetric salt conditions in the measurements of zeta potential. The positive magnitude of $A(2V)$ in Figure 4 for 0.1 mM/1 mM and 0.5 mM/5 mM $LiClO_4$ in (*R*)-PC could stem from the salt-concentration gradient leading to inhomogeneity of the local effective potential along the pore length, and possible nonlinear profiles of the EOF velocity.[83] The magnitude of $A(2V)$ might also be affected by diffusioosmosis.[84, 85] Our results therefore indicate that probing the polarity and magnitude of the effective potential of interfaces is more straightforward in symmetric electrolyte conditions. We also note that the possible origin of the lack of sensitivity of $A(2V)$ to the differences in the magnitude of the effective potential in high concentrations of $LiClO_4$ in *rac*PC and (*R*)-PC is that in our symmetric pores there is a threshold effective surface potential that leads to complete filling of the pore volume with the solution from one side of the pore for one voltage polarity, and with the solution from the other side for the opposite voltage polarity. As a result, the ion-current anisotropy could reach its maximum value and stay constant even if the effective potential increased.

Qualitatively similar findings of a higher positive potential present on silica and polymer surfaces in contact with *rac*PC point to the universal character of our findings. Our results indicate that electrochemical properties of solid–liquid interfaces are sensitive to the enantiomeric excess of the solvent even for surfaces that are not atomically flat.

3. Conclusions

Here we used nonlinear spectroscopic, electrochemical, and electrokinetic methods to probe and quantify the effective surface potential applicable to electrolyte solutions in PC. The two types of pores were used in the experiments, glass pipettes and

polymer pores, were subjected to $LiClO_4$ solutions prepared in (*R*)-PC and *rac*PC. I-V curves and streaming-current measurements pointed to the existence of finite effective surface charges in both types of pores that are dependent on the enantiomeric excess of the solvent and on the electrolyte concentrations. The accompanying spectroscopic measurements revealed that the effective surface potential is determined by a bilayer-like structure of the solvent that dictates the position of ions, and that the possible additional free volume in (*R*)-PC in comparison to *rac*PC enables ions to penetrate the surface bilayer in the former liquid at all electrolyte concentrations studied here.

We typically think of the non-chirality-dependent physical properties of the same material as being independent of enantiomeric excess, although some exceptions are known.[86] The work presented here shows that such a viewpoint might not be correct. Our experiments indicate that differences in the packing density of *rac*PC and (*R*)-PC are reflected in strikingly different electrochemical and electrokinetic behavior at a polar interface. This work underscores the need to develop a deeper understanding of the role of chirality at solid–liquid interfaces and suggests new approaches for improving ion transport in applications that involve interfaces in polar, aprotic organic solvents.

4. Acknowledgements

L.A.B and K.A. acknowledge the National Science Foundation award CHE-2220852 for support of this work. The Laganowsky laboratory at Texas A&M University is acknowledged for loan of the pressure-clamp rig. The use of Texas A&M University Microscopy and Imaging Center Core Facility (RRID: SCR_022128) is acknowledged. We acknowledge GSI Helmholtzzentrum für Schwerionenforschung in Darmstadt, Germany for providing irradiated membranes. The VSFG and experiments with PET pores were supported as part of the Center for Enhanced Nanofluidic Transport, an Energy Frontier Research Center funded by the U.S. Department of Energy, Office of Science, Basic Energy Sciences at the University of California, Irvine and the University of Maryland, College Park under award # DE-SC0019112.

5. References

[1] P. Jankowski, K. Grzegorzewska, A. Szabłowska, M. Piszcz, M. Dranka, G. Z. Żukowska, M. Kalita, *Electrochimica Acta* **2015**, *175*, 240-246.

[2] H. B. Park, J. Kamcev, L. M. Robeson, M. Elimelech, B. D. Freeman, *Science* **2017**, *356*, eaab0530.

[3] S. Sharma, P. Chand, *Results in Chemistry* **2023**, *5*, 100885.

[4] P. Marchetti, M. F. J. Solomon, G. Szekely, A. G. Livingston, *Chem Rev* **2014**, *114*, 10735-10806.

[5] R. Epsztein, R. M. DuChanois, C. L. Ritt, A. Noy, M. Elimelech, *Nature Nanotechnology* **2020**, *15*, 426-436.

[6] S. Howorka, Z. Siwy, *Chem Soc Rev* **2009**, *38*, 2360-2384.

[7] L. Xue, H. Yamazaki, R. Ren, M. Wanunu, A. P. Ivanov, J. B. Edel, *Nature Reviews Materials* **2020**, *5*, 931-951.

[8] R. P. Lively, D. S. Sholl, *Nat Mater* **2017**, *16*, 276-279.

[9] M. J. Zachman, Z. Tu, L. A. Archer, L. F. Kourkoutis, *ACS Energy Letters* **2020**, *5*, 1224-1232.

[10] Z. Zhu, D. Wang, Y. Tian, L. Jiang, *Journal of the American Chemical Society* **2019**, *141*, 8658-8669.

[11] G. H. Pollack, *Advances in colloid and interface science* **2003**, *103*, 173-196.

[12] F. M. Geiger, *The Journal of Physical Chemistry B* **2021**, *125*, 10401-10403.

[13] K. N. Olafson, R. J. Clark, P. G. Vekilov, J. C. Palmer, J. D. Rimer, *ACS Applied Materials & Interfaces* **2018**, *10*, 29288-29298.

[14] Y. Chen, L. Qing, T. Liu, S. Zhao, Y. Han, *Nano Energy* **2022**, *102*, 107660.

[15] X. Su, *Current Opinion in Colloid & Interface Science* **2020**, *46*, 77-93.

[16] B. Honig, A. Nicholls, *Science* **1995**, *268*, 1144-1149.

[17] J. N. Israelachvili, in *Intermolecular and Surface Forces (Third Edition)* (Ed.: J. N. Israelachvili), Academic Press, San Diego, **2011**, pp. 291-340.

[18] M. Tanaka, *Current Opinion in Colloid & Interface Science* **2013**, *18*, 432-439.

[19] R. B. Schoch, J. Y. Han, P. Renaud, *Rev Mod Phys* **2008**, *80*, 839-883.

[20] M. E. Davis, J. A. McCammon, *Chem Rev* **1990**, *90*, 509-521.

[21] R. M. M. Smeets, U. F. Keyser, D. Krapf, M. Y. Wu, N. H. Dekker, C. Dekker, *Nano Lett* **2006**, *6*, 89-95.

[22] A. Alcaraz, E. M. Nestorovich, M. Aguilella-Arzo, V. M. Aguilella, S. M. Bezrukov, *Biophysical Journal* **2004**, *87*, 943-957.
[23] R. Qi, R. Luo, *Journal of Chemical Information and Modeling* **2019**, *59*, 409-420.
[24] G. Feng, J. Huang, B. G. Sumpter, V. Meunier, R. Qiao, *Physical Chemistry Chemical Physics* **2010**, *12*, 5468-5479.
[25] Y. Cui, T.-S. Chung, *Nature Communications* **2018**, *9*, 1426.
[26] Z. Hu, J. D. Weeks, *The Journal of Physical Chemistry C* **2010**, *114*, 10202-10211.
[27] S. Liu, Z. Hu, J. D. Weeks, J. T. Fourkas, *The Journal of Physical Chemistry C* **2012**, *116*, 4012-4018.
[28] A. Mendhe, H. S. Panda, *Discover Materials* **2023**, *3*, 29.
[29] D. Ren, S. Ren, Y. Lin, J. Xu, X. Wang, *Chemosphere* **2021**, *271*, 129425.
[30] Z. P. Cano, D. Banham, S. Y. Ye, A. Hintennach, J. Lu, M. Fowler, Z. W. Chen, *Nature Energy* **2018**, *3*, 279-289.
[31] L. S. Roselin, R. S. Juang, C. T. Hsieh, S. Sagadevan, A. Umar, R. Selvin, H. H. Hegazy, *Materials* **2019**, *12*.
[32] M. S. Whittingham, *Nano Lett* **2020**, *20*, 8435-8437.
[33] J. W. Polster, A. J. Souna, M. H. Motevaselian, R. A. Lucas, J. D. Tran, Z. S. Siwy, N. R. Aluru, J. T. Fourkas, *Natural Sciences* **2022**, *2*, e20210099.
[34] A. J. Souna, M. H. Motevaselian, J. W. Polster, J. D. Tran, Z. S. Siwy, N. R. Aluru, J. T. Fourkas, *Physical Chemistry Chemical Physics* **2024**, *26*, 6726-6735.
[35] B. J. Berne, J. T. Fourkas, R. A. Walker, J. D. Weeks, *Accounts of Chemical Research* **2016**, *49*, 1605-1613.
[36] R. A. Lucas, C.-Y. Lin, Z. S. Siwy, *The Journal of Physical Chemistry B* **2019**, *123*, 6123-6131.
[37] Y. H. Qiu, R. A. Lucas, Z. S. Siwy, *J Phys Chem Lett* **2017**, *8*, 3846-3852.
[38] S. Silva, S. Singh, E. Cao, J. T. Fourkas, Z. S. Siwy, *Faraday Discussions* **2023**, *246*, 508-519.
[39] C. A. Rivera, J. S. Bender, K. Manfred, J. T. Fourkas, *J Phys Chem A* **2013**, *117*, 12060-12066.
[40] C. Wei, A. J. Bard, S. W. Feldberg, *Analytical Chemistry* **1997**, *69*, 4627.
[41] H. S. White, A. Bund, *Langmuir* **2008**, *24*, 2212.
[42] S. Umehara, N. Pourmand, C. D. Webb, R. W. Davis, K. Yasuda, M. Karhanek, *Nano Lett* **2006**, *6*, 2486-2492.
[43] T. Plett, W. Q. Shi, Y. H. Zeng, W. Mann, I. Vlassiouk, L. A. Baker, Z. S. Siwy, *Nanoscale* **2015**, *7*, 19080-19091.
[44] F. H. J. van der Heyden, D. Stein, K. Besteman, S. G. Lemay, C. Dekker, *Physical Review Letters* **2006**, *96*, 224502.
[45] R. L. Fleischer, P. B. Price, R. M. Walker, R. M. Walker, *Nuclear Tracks in Solids: Principles and Applications*, University of California Press, **1975**.
[46] S. Müller, C. Schötz, O. Picht, W. Sigle, P. Kopold, M. Rauber, I. Alber, R. Neumann, M. E. Toimil-Molares, *Crystal Growth & Design* **2012**, *12*, 615-621.
[47] T. Fujinaga, K. Izutsu, *Pure and Applied Chemistry* **1971**, *27*, 273-280.
[48] R. Spohr, **1983**.
[49] P. Y. Apel, Y. E. Korchev, Z. Siwy, R. Spohr, M. Yoshida, *Nuclear Instruments and Methods in Physics Research Section B: Beam Interactions with Materials and Atoms* **2001**, *184*, 337-346.
[50] P. Apel, *Radiat. Meas.* **2001**, *34*, 559-566.
[51] M. Buck, M. Himmelhaus, *Journal of Vacuum Science & Technology A* **2001**, *19*, 2717-2736.
[52] F. Vidal, A. Tadjeddine, *Reports on Progress in Physics* **2005**, *68*, 1095.
[53] L. Yang, B. H. Fishbine, A. Migliori, L. R. Pratt, *The Journal of Chemical Physics* **2010**, *132*, 044701.
[54] F. Ding, Z. Hu, Q. Zhong, K. Manfred, R. R. Gattass, M. R. Brindza, J. T. Fourkas, R. A. Walker, J. D. Weeks, *The Journal of Physical Chemistry C* **2010**, *114*, 17651-17659.
[55] F. Ding, Q. Zhong, K. Manfred, X. He, J. S. Bender, M. R. Brindza, R. A. Walker, J. T. Fourkas, *The Journal of Physical Chemistry C* **2012**, *116*, 4019-4025.
[56] H. T. Jiang, Q. Zhang, Y. T. Zhang, L. Z. Sui, G. R. Wu, K. J. Yuan, X. M. Yang, *Physical Chemistry Chemical Physics* **2019**, *21*, 10417-10422.
[57] K. Kondo, M. Sano, A. Hiwara, T. Omi, M. Fujita, A. Kuwae, M. Iida, K. Mogi, H. Yokoyama, *J. Phys. Chem. B* **2000**, *104*, 5040-5044.
[58] A. Brodin, P. Jacobsson, *Journal of Molecular Liquids* **2011**, *164*, 17-21.
[59] M. I. Chaudhari, A. Muralidharan, L. R. Pratt, S. B. Rempe, *Modeling Electrochemical*

Energy Storage at the Atomic Scale **2018**, 53-77.
[60] Propylene carbonate information sheet, Merck KGaA, Darmstadt, Germany and/or its affiliates., accessed 02 May 2024, https://www.sigmaaldrich.com/US/en/product/sial/310328#product-documentation.
[61] (R)-(+)-Propylene carbonate information sheet, Merck KGaA, Darmstadt, Germany and/or its affiliates, accessed 02 May 2024, https://www.sigmaaldrich.com/US/en/product/aldrich/540013.
[62] G. Caniglia, G. Tezcan, G. N. Meloni, P. R. Unwin, C. Kranz, *Annual Review of Analytical Chemistry* **2022**, *15*, 247-267.
[63] N. Sa, L. A. Baker, *Journal of the Electrochemical Society* **2013**, *160*, H376-H381.
[64] N. Sa, W. J. Lan, W. Q. Shi, L. A. Baker, *ACS Nano* **2013**, *7*, 11272-11282.
[65] Z. S. Siwy, S. Howorka, *Chem Soc Rev* **2010**, *39*, 1115-1132.
[66] M. Ali, P. Ramirez, S. Mafé, R. Neumann, W. Ensinger, *ACS Nano* **2009**, *3*, 603-608.
[67] X. Hou, W. Guo, L. Jiang, *Chem Soc Rev* **2011**, *40*, 2385-2401.
[68] Z. Zhang, X. Huang, Y. Qian, W. Chen, L. Wen, L. Jiang, *Advanced Materials* **2020**, *32*, 1904351.
[69] C. Wei, A. J. Bard, S. W. Feldberg, *Anal. Chem.* **1997**, *69*, 4627-4633.
[70] E. A. Heins, L. A. Baker, Z. S. Siwy, M. O. Mota, C. R. Martin, *The Journal of Physical Chemistry B* **2005**, *109*, 18400-18407.
[71] Z. Siwy, E. Heins, C. C. Harrell, P. Kohli, C. R. Martin, *Journal of the American Chemical Society* **2004**, *126*, 10850-10851.
[72] H. S. White, A. Bund, *Langmuir* **2008**, *24*, 2212-2218.
[73] J. Cervera, B. Schiedt, R. Neumann, S. Mafé, P. Ramírez, *The Journal of Chemical Physics* **2006**, *124*.
[74] D. C. Martins, V. Chu, D. M. F. Prazeres, J. P. Conde, *Microfluidics and Nanofluidics* **2013**, *15*, 361-376.
[75] M. Castelain, F. Pignon, J.-M. Piau, A. Magnin, *The Journal of Chemical Physics* **2008**, *128*.
[76] Y. Gu, D. Li, *Journal of Colloid and Interface Science* **2000**, *226*, 328-339.
[77] N. Peruzzi, P. Lo Nostro, B. W. Ninham, P. Baglioni, *Journal of Solution Chemistry* **2015**, *44*, 1224-1239.
[78] A. Wolf, N. Reber, P. Y. Apel, B. E. Fischer, R. Spohr, *Nuclear Instruments and Methods in Physics Research Section B: Beam Interactions with Materials and Atoms* **1995**, *105*, 291-293.
[79] M. R. Powell, I. Vlassiouk, C. Martens, Z. S. Siwy, *Physical Review Letters* **2009**, *103*, 248104.
[80] L. Renaud, P. Kleimann, P. Morin, *Electrophoresis* **2004**, *25*, 123-127.
[81] B. J. Kirby, E. F. Hasselbrink Jr., *Electrophoresis* **2004**, *25*, 187-202.
[82] P. Saha, C. Nam, M. A. Hickner, I. V. Zenyuk, *The Journal of Physical Chemistry C* **2019**, *123*, 19493-19505.
[83] R. Peng, D. Q. Li, *Journal of Colloid and Interface Science* **2015**, *440*, 126-132.
[84] H. J. Keh, Y. K. Wei, *Journal of Colloid and Interface Science* **2002**, *252*, 354-364.
[85] J. H. Wu, H. J. Keh, *Colloid Surf. A-Physicochem. Eng. Asp.* **2003**, *212*, 27-42.
[86] C. P. Brock, W. B. Schweizer, J. D. Dunitz, *Journal of the American Chemical Society* **1991**, *113*, 9811-9820.